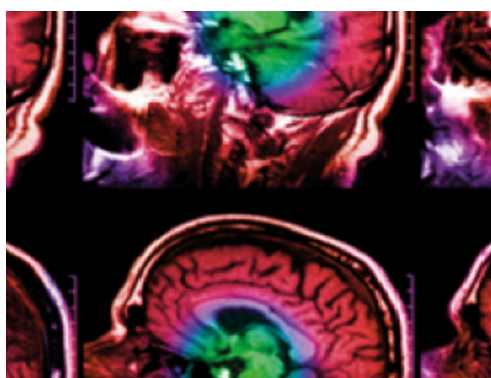


PAPER • OPEN ACCESS

## Brachytherapy treatment verification using gamma radiation from the internal treatment source combined with an imaging panel—a phantom study

To cite this article: G P Fonseca *et al* 2021 *Phys. Med. Biol.* **66** 104001

View the [article online](#) for updates and enhancements.



**IPEM | IOP**

Series in Physics and Engineering in Medicine and Biology

Your publishing choice in medical physics,  
biomedical engineering and related subjects.

Start exploring the collection—download the  
first chapter of every title for free.



## PAPER

## OPEN ACCESS


RECEIVED  
17 January 2021REVISED  
27 March 2021ACCEPTED FOR PUBLICATION  
8 April 2021PUBLISHED  
5 May 2021

Original content from this work may be used under the terms of the [Creative Commons Attribution 4.0 licence](#).

Any further distribution of this work must maintain attribution to the author(s) and the title of the work, journal citation and DOI.



# Brachytherapy treatment verification using gamma radiation from the internal treatment source combined with an imaging panel—a phantom study

G P Fonseca<sup>1,3,\*</sup> , T van Wagenberg<sup>1,3</sup> , R Voncken<sup>1</sup>, M Podesta<sup>1</sup>, C van Beveren<sup>1</sup>, E van Limbergen<sup>1</sup>, L Lutgens<sup>1</sup>, B Vanneste<sup>1</sup>, M Berbee<sup>1</sup>, B Reniers<sup>2</sup> and F Verhaegen<sup>1</sup>

<sup>1</sup> Department of Radiation Oncology (MAASTRO), GROW School for Oncology and Developmental Biology, Maastricht University Medical Centre+, Doctor Tanslaan 12, 6229 ET Maastricht, The Netherlands

<sup>2</sup> Research group NuTeC, Centre for Environmental Sciences, Hasselt University, Diepenbeek, Belgium

<sup>3</sup> Both authors contributed equally to this manuscript.

\* Author to whom any correspondence should be addressed.

E-mail: [gabriel.paivafonseca@maastro.nl](mailto:gabriel.paivafonseca@maastro.nl)

**Keywords:** brachytherapy, *in vivo* dosimetry, imaging panel, 3D printed phantom

## Abstract

Brachytherapy has an excellent clinical outcome for different treatment sites. However, *in vivo* treatment verification is not performed in the majority of hospitals due to the lack of proper monitoring systems. This study investigates the use of an imaging panel (IP) and the photons emitted by a high dose rate (HDR) <sup>192</sup>Ir source to track source motion and obtain some information related to the patient anatomy. The feasibility of this approach was studied by monitoring the treatment delivery to a 3D printed phantom that mimicks a prostate patient. A 3D printed phantom was designed with a template for needle insertion, a cavity ('rectum') to insert an ultrasound probe, and lateral cavities used to place tissue-equivalent materials. CT images were acquired to create HDR <sup>192</sup>Ir treatment plans with a range of dwell times, interdwell distances and needle arrangements. Treatment delivery was verified with an IP placed at several positions around the phantom using radiopaque markers on the outer surface to register acquired IP images with the planning CT. All dwell positions were identified using acquisition times  $\leq 0.11$  s (frame rates  $\geq 9$  fps). Interdwell distances and dwell positions (in relation to the IP) were verified with accuracy better than 0.1 cm. Radiopaque markers were visible in the acquired images and could be used for registration with CT images. Uncertainties for image registration (IP and planning CT) between 0.1 and 0.4 cm. The IP is sensitive to tissue-mimicking insert composition and showed phantom boundaries that could be used to improve treatment verification. The IP provided sufficient time and spatial resolution for real-time source tracking and allows for the registration of the planning CT and IP images. The results obtained in this study indicate that several treatment errors could be detected including swapped catheters, incorrect dwell times and dwell positions.

## 1. Introduction

High dose rate (HDR) brachytherapy has an excellent clinical outcome for different treatment sites (Sturdza *et al* 2016, Vanneste *et al* 2016, Zaorsky *et al* 2017, Astrom *et al* 2018, Crook *et al* 2020). However, compared to external beam radiotherapy, this technique is more susceptible to treatment errors due to the significant number of manual steps in the clinical workflow and steep dose gradients. According to the International Commission on Radiological Protection (Valentin 2005), the majority of the incidents reported by 2004 could have been avoided if staff had proper monitoring equipment. Incidents are still being reported frequently (Fonseca *et al* 2019). *In vivo* dosimetry (IVD) is not implemented by the majority of the radiotherapy centers (Tanderup *et al* 2006) due to laborious or impractical methods, lack of equipment and high measurement uncertainties

(Fonseca *et al* 2020). Most treatment verification studies available in the literature (Alecú and Alecú 1999, Brezovich *et al* 2000, Anagnostopoulos *et al* 2003, Nose *et al* 2005, Waldhausl *et al* 2005, Cygler *et al* 2006, Das *et al* 2007, Toye *et al* 2009, Allahverdi *et al* 2012, Sharma and Jursinic 2013, Carrara *et al* 2017, Jaselske *et al* 2017, Melchert *et al* 2018) used point dosimeters and evaluated the time-integrated dose. Integrated point doses are dominated by dwell positions in the vicinity of the detector, and therefore can be very insensitive to deviations in dwell positions further away from the detector. Time-resolved detectors and source tracking have shown promising results (Guiral *et al* 2016, Mason *et al* 2016, Fonseca *et al* 2017a, Belley *et al* 2018, Johansen *et al* 2018, Smith *et al* 2018), increasing the likelihood to detect treatment errors by a at least a factor of ten (Andersen *et al* 2009). Imaging immediately before treatment delivery reduces measurement deviations (Suchowerska *et al* 2011, Carrara *et al* 2017), although in-room imaging is not yet a reality for most clinics. A recently published ESTRO Task Group report, which includes a literature review (Fonseca *et al* 2020), describes advantages of source tracking and time-resolved measurements, and defines some requirements and future directions for IVD in brachytherapy.

This study evaluates the use of an imaging panel (IP) for treatment verification in  $^{192}\text{Ir}$  HDR brachytherapy using a 3D printed anthropomorphic phantom to mimic treatment conditions. The use of an IP for source tracking has been described for homogeneous phantoms (Smith *et al* 2013, Fonseca *et al* 2017a), applicator commissioning (Fonseca *et al* 2017b), and imaging in contrast phantoms (Verhaegen *et al* 2007). This is the first study to report the use of geometric and anatomical information projected by the  $^{192}\text{Ir}$  source onto the IP for a realistic anthropomorphic phantom, and the effect of IP settings (e.g. acquisition rate and distance between source and detector).

## 2. Methods and materials

This study focusses on the measurement of dwell times, dwell positions, and image registration to verify brachytherapy using planning CT images as a reference. This section describes the anthropomorphic phantom manufactured for this study, the experimental setup and methodology employed to evaluate dwell times, dwell positions and geometric/anatomical information. The combination of time-resolved information about source tracking, geometrical imaging (markers) and anatomical imaging generates a tremendous amount of data that can be processed in different ways. Figure 1 shows how we envision the use of the proposed method in a clinical workflow.

### 2.1. Prostate phantom

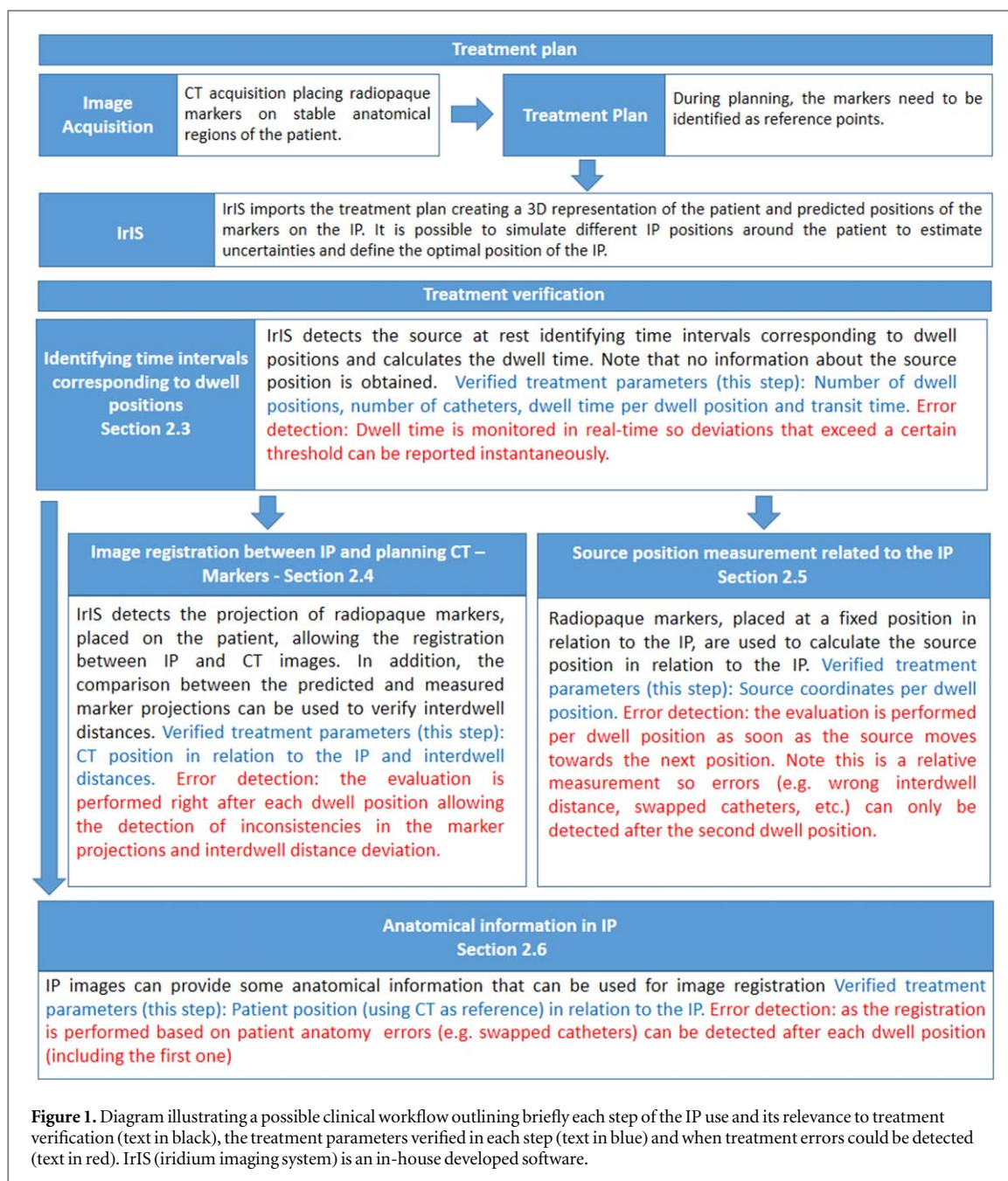
A life-size 3D printed pelvic phantom (figure 2(a)), based on a CT image of a brachytherapy prostate patient, was designed with 4 holes for the insertion of tissue-mimicking inserts (TMI), a 'rectum' air cavity for the insertion of a transrectal ultrasound (US) probe (BK Medical, Herlev Denmark), and a template (9 × 9 channels in 1 cm intervals) for needle insertion. Plastic needles, enabling insertion of the brachytherapy source, are placed into the phantom that allows for several implant configurations to mimic treatments. The phantom was printed with a fused filament fabrication printer using a PLA + (C<sub>3</sub>H<sub>4</sub>O<sub>2</sub>) filament (Zhuhai Sunlu Industrial co., Ltd, Zhuhai, China) to mimic soft tissue characteristics. The printed model has a density of 1.05 g · cm<sup>-3</sup>.

### 2.2. Experimental setup

Figure 2(a) shows the prostate phantom with 7 needles, 4 TMI (GAMMEX, Middleton, USA) and an US probe, jointly placed on top of an IP model PAXSCAN 2530HE (Varex Imaging, Salt Lake City, USA). Experiments were performed with different configurations (e.g. different needle arrangements and different TMI) as described in table 1. Radiopaque markers consisting of covered lead spheres with 0.15 (standard for the patients in our clinic), 0.30 and 0.50 cm total diameters were attached to the surface of the phantom for image registration (see section 2.4). A CT image (figure 2(b)) was used to create treatment plans with the BrachyVision, version 15, treatment planning system (Varian Medical Systems, Palo Alto, USA).

Experiments were performed using a 3D printed holder (visible in figure 4) manufactured to place the IP at specific distances and angles around the phantom to ensure stability and reproducibility. The effect of the IP position was evaluated for 10 and 20 cm distances between the surface of the patient and the IP, and at 3 different angles (0°, 45°, and 90°) as illustrated in figure 2(c). The distances were selected considering a future clinical application where the IP may be placed in the treatment table underneath the patient. Cushioning and a support frame will be installed between the IP and the patient, meaning 10 cm is the estimated shortest distance whilst 20 cm represents a worst-case scenario tested to verify the sensitivity of the IP.

The IP used in this study has a DRZ Plus conversion screen with a wide energy range (20 kV–16 MV) and a sensitive area of 24.5 × 30.2 cm<sup>2</sup> composed of 1792 × 2176 pixels. The electronics are protected by internal shielding designed for up to 225 kV. High spatial resolution mode (0.0139 cm per pixel) allows up to 9 fps,

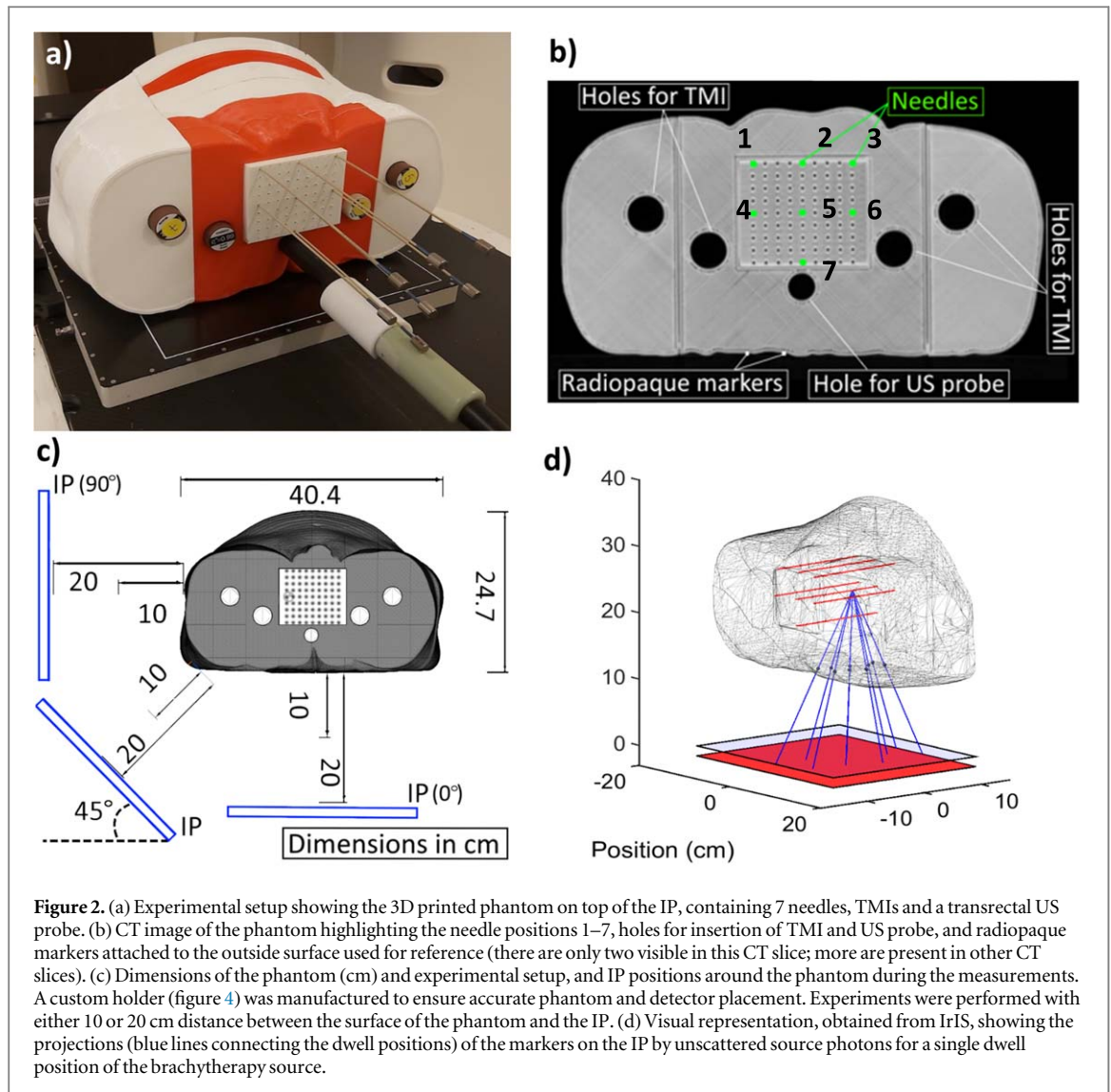


whereas  $2 \times 2$  pixel binning mode (0.027 cm per pixel) allows up to 33 fps. There are also different gain options for each acquisition mode, which can be adjusted depending on the source air-kerma strength and distance between the source and the IP. In-house developed software, called IrIS (Iridium Imaging System), is used to process and acquire the data. Images are continually acquired and recorded if the intensity is above a pre-defined threshold (background level). Therefore, frames are automatically stored once the source leaves the afterloader. The file size per frame is 1.9 MB and 7.4 MB for low and high-resolution mode, respectively. A fifteen minutes treatment would generate up to 8100 frames (9 fps) and 29700 frames (33 fps) equivalent to approximately 55 GB of data. Storage limitations and the computational time to process the data have been taken into account during the evaluation of the results.

### 2.3. Dwell time

The intensity difference per pixel between consecutive IP frames is calculated by creating a 2D difference map with visible cold and hot spots if the source position has changed between the frames. The total absolute intensity difference ( $T_{Dif}$ ) between consecutive frames ( $\mathbf{k}$ ) is calculated (equation (1)).  $N_x$  and  $N_y$  are the number of pixels in the X and Y directions, respectively.  $F$  represents each frame with acquisition index  $k$  and  $ij$  are the coordinates of each pixel





$$T_{Dif}(k) = \sum_{i=1}^{N_x} \sum_{j=1}^{N_y} |F(k+1)_{ij} - F(k)_{ij}|. \quad (1)$$

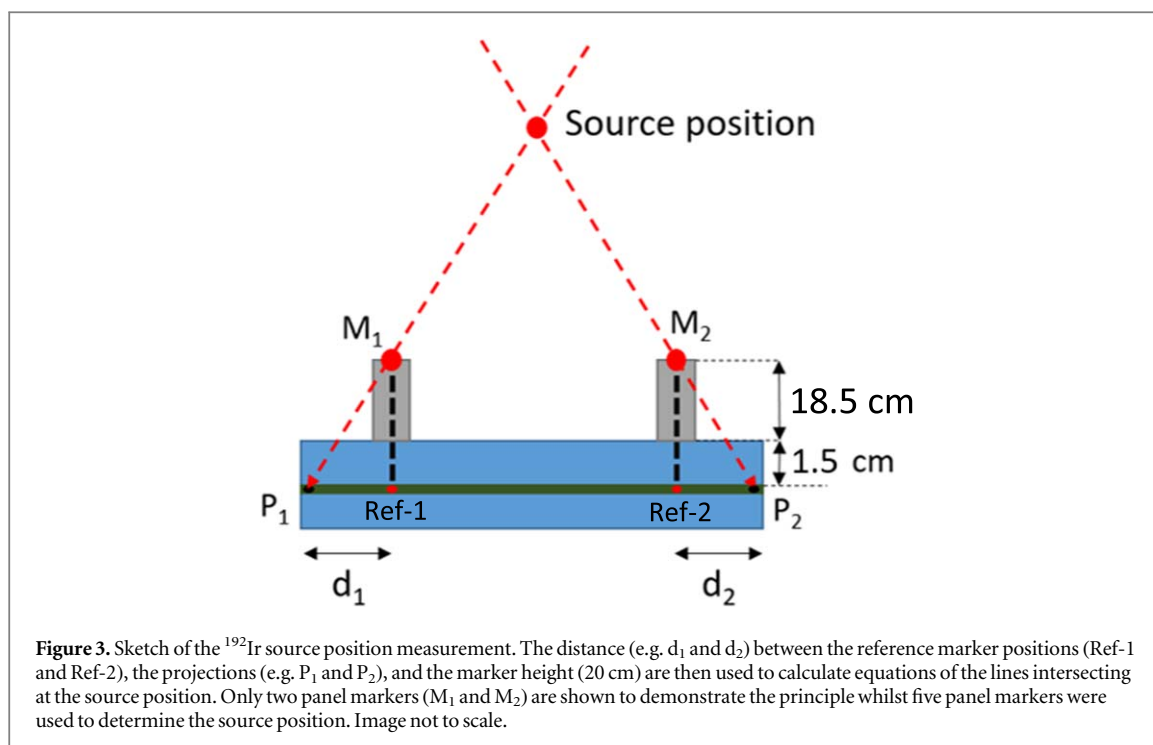
The IrIS user interface evaluates the total difference vector, identifying large gradients corresponding to source movements.  $T_{Dif}$  is small (pixel response variation mostly from noise) if the source is at rest whilst much larger  $T_{Dif}$  values (pixel response variation mostly due to the source displacement) are obtained when the source is moving. IrIS identifies when the source is moving (peaks in the  $T_{Dif}$  vector) and which frames correspond to the same dwell position. The acquisition time of each frame is used to determine dwell times. Note that a transit time due to the source approaching the first dwell position, moving between dwell positions and returning to the safe may or may not be accounted for depending on the acquisition rate. The transit time is defined in this study as the time interval spent by the source while moving between two consecutive dwell positions. The transit time correction applied in this study consist of the subtraction of frames where the source was moving between dwell positions.

#### 2.4. Image registration, marker size and interdwell distance

A CT image of the phantom (figure 2(b)), with markers attached to the outside surface, is used as a reference to create a treatment plan and calculate the projected position of each radiopaque marker on the IP. IrIS was integrated with AMIGO (A Medical Image-based Graphical platfOrm) (Fonseca *et al* 2014) to import the treatment plan and create a projection map of the patient markers. IrIS considers the  $^{192}\text{Ir}$  source as a point source and calculates the projection of each patient marker on the IP, using Euclidian geometry as illustrated in figure 2(d).

**Table 1.** Experimental setup and IP settings. Measurements were repeated for each acquisition rate corresponding to 20 different experimental setups and 4 acquisition rates for each experiment totaling 80 measurements. Besides the frame rate and pixel resolution, the IP gain was adjusted for each distance between the source and the IP. Experiments were performed using a GammaMed Plus iX afterloader (Varian Medical Systems, Palo Alto, CA) equipped with a GammaMed Plus HDR 192Ir source (Ballester *et al* 2001).

Experimental settings—overview	
Dwell times	0.3, 0.5, and 1 s
Interdwell distances	0.1, 0.2, 0.3, and 0.5 cm
Distance between phantom surface and IP	From 10 up to 20 cm
Distance between source and IP	From 17.5 up to 47 cm. Minimum distance for the IP at 0° and maximum for the IP at 45°.
Angle around the phantom	0°, 45° and 90°
Radiopaque markers	0.15, 0.30 and 0.50 cm total diameter
Tissue mimicking inserts (Gammex)	Inflated lung (0.30 g cm <sup>-3</sup> ), adipose (0.95 g cm <sup>-3</sup> ), solid water (1.02 g cm <sup>-3</sup> ), muscle (1.05 g cm <sup>-3</sup> ), inner bone (1.13 g cm <sup>-3</sup> ), bone mineral (1.15 g cm <sup>-3</sup> ), CB2%-30% CaCo <sub>3</sub> (1.33 g cm <sup>-3</sup> ), CB2%-50% CaCo <sub>3</sub> (1.56 g cm <sup>-3</sup> ) and cortical bone (1.82 g cm <sup>-3</sup> )
IP settings	
IP acquisition rate/resolution	5 and 9 fps (pixel resolution 0.0139 cm) 5, 9, 20 and 33 fps (pixel resolution 0.0278 cm)
Experimental settings—specific experiments	
Experiment 1: Dwell time	7 needles as shown in figures 2(a), (b) 30 dwell positions per needle equally distributed into 0.3, 0.5 and 1.0 s dwell time Fixed interdwell distance of 0.3 cm Measurements performed with 10 and 20 cm distance between the IP and the surface of the phantom with the phantom at 0° 9 fps (pixel resolution 0.0139 cm) and 5, 9, 20 and 33 fps (pixel resolution 0.0278 cm) Air-kerma strength 41514U
Experiment 2: Marker size	7 needles as shown in figures 2(a), (b) Several markers (>10) with different diameters were placed on the surface of the phantom 0.2 cm interdwell distance 10 dwell positions per needle with a 1s dwell time each Measurements performed with 10 and 20 cm distance between the IP and the surface of the phantom for the IP at 0° 9 and 20 fps (pixel resolution 0.0278 cm) Air-kerma strength 31746U
Experiment 3: Image registration and interdwell distance	7 needles as shown in figures 2(a), (b)  A fixed dwell time of 1 s 10 consecutive positions with 0.1 cm interdwell distance, followed by 5 dwell position with 0.2 cm interdwell distance and 6 dwell positions with 0.5 cm interdwell distance totaling 21 dwell positions per needle Measurements performed with 10 and 20 cm distance between the IP and the surface of the phantom for the IP at 0°, 45° and 90° 9 and 20 fps (pixel resolution 0.0278 cm) Air-kerma strength 41514U
Experiment 4: Dwell positions in relation to the IP	A fixed dwell time of 1 s  Measurements performed at 20 cm distance between the IP and the surface of the phantom for the IP at 0° 10 fps (pixel resolution 0.0278 cm) Air-kerma strength 41514U 2 different interdwell distances (0.2 and 0.5 cm) were tested separately using 7 needles as shown in figure 2(a)
Experiment 5: Imaging TMI	3 needles as shown in figure 4 1 dwell position with a 3 s dwell time per insert. A 12.5 cm offset from the tip of the needle was used so the dwell position depth was approximately at the middle of the insert The distance between the IP and the surface of the phantom was adjusted to 10 cm whilst the distance between the source and the IP was 29.5 cm 5 fps (pixel resolution 0.0278 cm) Measurements performed with 10 cm distance between the detector and the surface of the phantom for the IP at 90° Air-kerma strength 41514U



#### 2.4.1. Marker size

Radiopaque markers were evaluated, consisting of lead spheres with 0.15, 0.30 and 0.50 cm diameters. Because of their spherical shape and the irradiation angle, projections on the IP appear as ellipses (approximated as circles due to the small size of the markers) and thus a Hough transform-based algorithm can be used to determine the position of the center and size of the markers. The patient markers were placed on the outside surface of the phantom in groups of three (each group consists of one marker of each size) in the same region to compare their projections under the same conditions. As the marker detection algorithm works better when optimized for a specific marker size, the results of these irradiations were used to select one diameter that was used in the remaining experiments.

#### 2.4.2. Image registration and interdwel distance

The patient markers (only 0.30 cm markers were used in this section) should be placed on stable anatomical regions (e.g. where bone structures are more pronounced) so the position of the IP needs to be optimized to visualize the projections. An interactive interface in IrIS allows the simulation of the IP at different angles and positions around the CT geometry. The projection map based on the CT markers is used as a reference to register CT and IP coordinates so that the measured position can be related to the patient anatomy. In addition to image registration, patient marker projections were used to verify interdwel distances by comparing the displacement of the measured projections in two consecutive dwell positions against predicted values obtained with IrIS. Deviations from the expected value can indicate geometrical (e.g. patient shift in relation to the IP) or treatment errors (e.g. a shifted catheter/appliator within the applicator). The resolution of the images is lowered before applying the algorithm to improve speed and reduce noise (Atherton and Kerbyson 1999).

### 2.5. Dwell positions related to the IP

Reference markers fixed at known positions compared to the IP provide more reliable information on the location of the source relative to the panel, than the markers on the patient that were used for registration (section 2.4.2), because their position is more stable. Therefore, it was decided to use a second set of markers (panel markers), at a fixed position in relation to the panel, to reconstruct the dwell positions using backprojection (see figure 3 and section 3.2.2). This method allows for the verification of the implant geometry and delivery sequence, which is independent of the image registration and patient anatomy. A 3D printed holder was used to place multiple radiopaque markers at defined positions 20 cm above the active layer of the panel. The HDR  $^{192}\text{Ir}$  source position is then obtained by solving a linear equation between each panel marker (physical position) and its respective projection on the IP and finding the intersection between the lines obtained for different panel markers (figure 3). This backprojection approach uses the same method as described in section 2.4 (figure 2(d)) to predict the projection of the patient markers, but in the reverse order, using measured projection to calculate the source position.

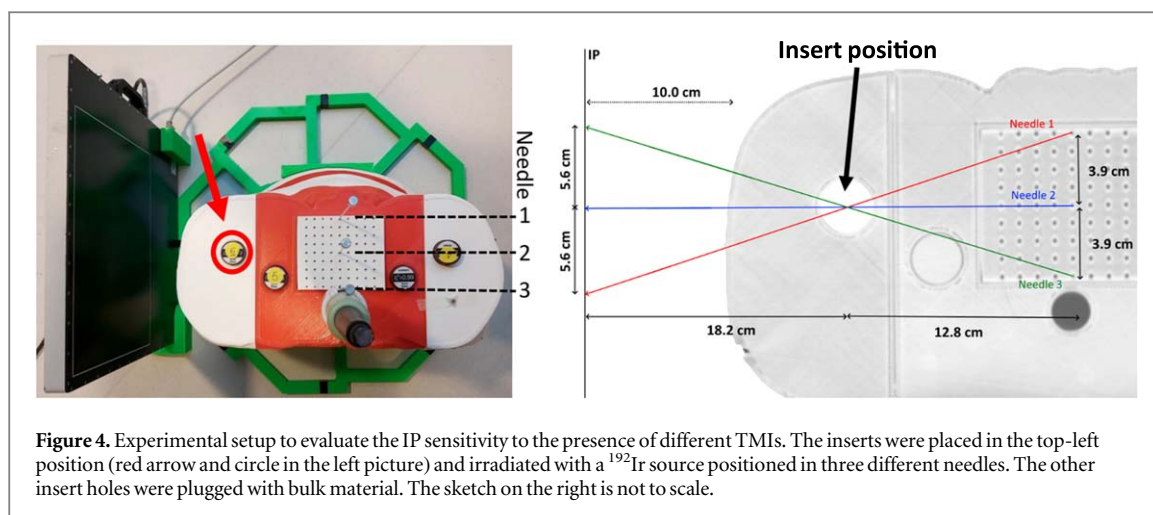


**Figure 4.** Experimental setup to evaluate the IP sensitivity to the presence of different TMIs. The inserts were placed in the top-left position (red arrow and circle in the left picture) and irradiated with a  $^{192}\text{Ir}$  source positioned in three different needles. The other insert holes were plugged with bulk material. The sketch on the right is not to scale.

## 2.6. Tissue mimicking inserts

Patient positioning relative to the IP is the main challenge since brachytherapy treatment rooms are usually not equipped with patient tracking devices, lasers for positioning, or in-room imaging. Therefore, source position measurements are usually performed in relation to the detector. In this study, in addition to evaluating the use of external markers, we also explored the possibility to use the patient anatomy projected on the IP to find the position of the patient with respect to the IP. The sensitivity of the IP to different photon-absorbing materials was evaluated by placing TMIs (table 1) into the phantom with a 10 cm distance between the IP and the surface of the phantom (figure 4). The IP response is dominated by scattered photons, so response variations due to the material composition and density are difficult to observe without postprocessing. The absolute response of the panel was evaluated for the different materials and also normalized to results obtained with the solid water insert. The normalization approach is only possible with phantoms and was used to enhance differences in the IP response. In addition, IP images were evaluated by subtracting the results obtained with the source in needle 1 and 3 by the results obtained using needle 2. We hypothesize that scatter can be similar for different dwell position whilst anatomical/geometrical information from primary photons can differ significantly. Therefore, IP signals from a dwell position could possibly be used as a type of scatter correction for a different dwell position.

## 3. Results

### 3.1. Dwell time

The total intensity difference of a frame compared to its previous frame ( $T_{Dif}(k)$ ), defined in equation (1), shows well-defined peaks as a function of time indicating positions where the source is moving. Figure 5 shows results obtained with the IP at 20 cm from the phantom surface ( $0^\circ$ ) using a 20 fps acquisition rate. The triangles indicate detected peaks, indicating source movement either between dwell positions (red triangles) or coming from and returning to the safe (blue triangles). Vertical dashed lines indicate when source movement was detected ( $T_{Dif}$  peaks) followed by a valley (low and stable  $T_{Dif}$  values indicating the source is at rest). The information is used to calculate dwell times and define which frames were obtained at the same dwell position.

The dwell time can be defined as the time interval between consecutive peaks (figures 5(a), (b)) that includes the dwell time and the transit time due to the source moving between consecutive dwell positions. Nevertheless, higher acquisition rates can distinguish between the actual dwell time (source at rest) from the transit time. The frames around the peaks (figure 5(c))—between dashed vertical lines) have higher  $T_{Dif}$  values indicating the source is moving. These frames can be disregarded so the dwell time corresponds to the length of a valley between two consecutive peaks (dwell time only). The absolute transit time is about 0.15 s for a 0.3 cm interdwell distance.

IrIS automatic dwell detection works for most of the cases, however, some parameters depend on the frame rate and distance between the IP and patient. All the post-processing parameters (e.g. the threshold for peak detection and a minimum number of frames at rest to define a dwell position) can be adjusted interactively using IrIS.



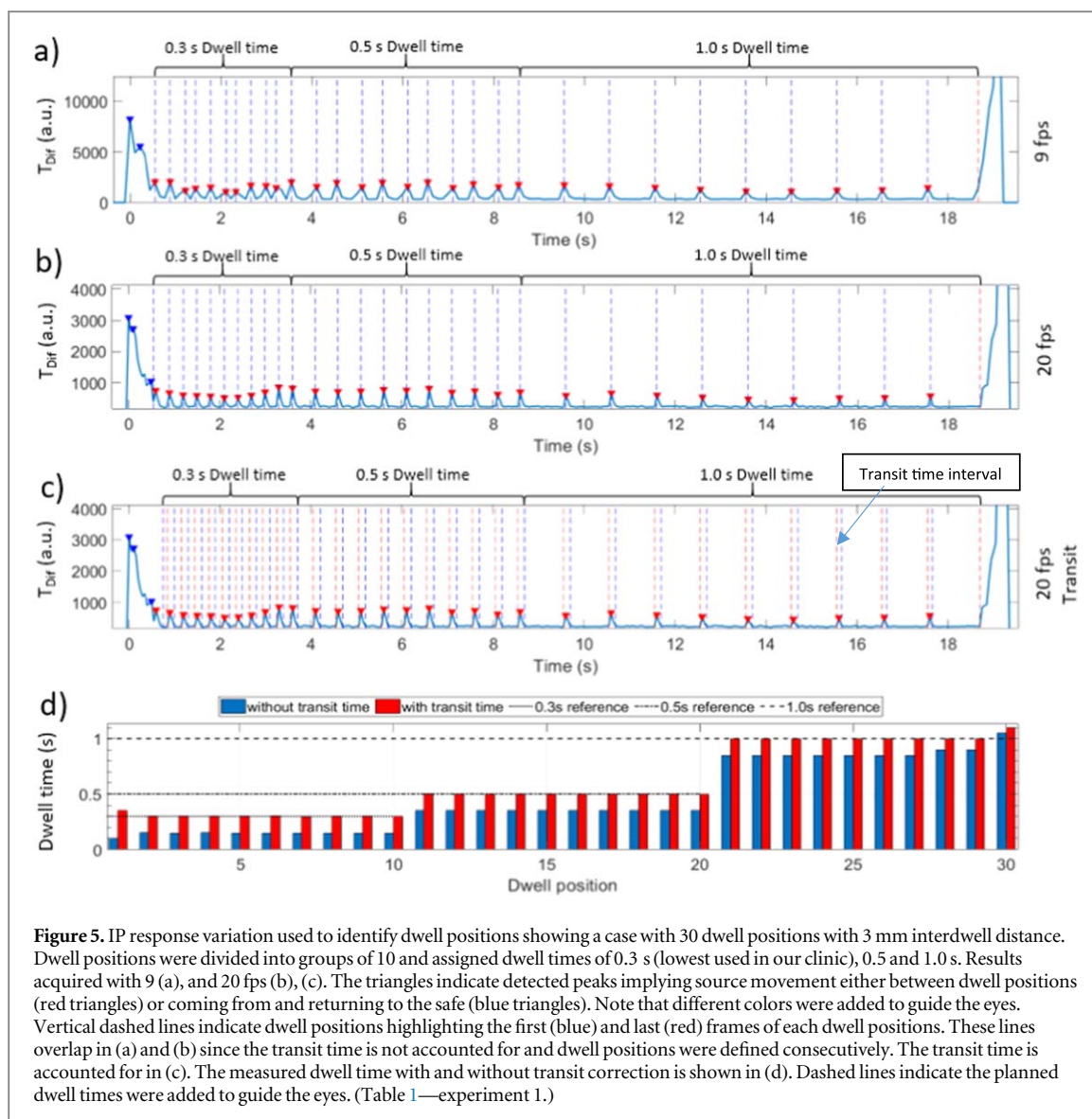


**Figure 5.** IP response variation used to identify dwell positions showing a case with 30 dwell positions with 3 mm interdwell distance. Dwell positions were divided into groups of 10 and assigned dwell times of 0.3 s (lowest used in our clinic), 0.5 and 1.0 s. Results acquired with 9 (a), and 20 fps (b), (c). The triangles indicate detected peaks implying source movement either between dwell positions (red triangles) or coming from and returning to the safe (blue triangles). Note that different colors were added to guide the eyes. Vertical dashed lines indicate dwell positions highlighting the first (blue) and last (red) frames of each dwell positions. These lines overlap in (a) and (b) since the transit time is not accounted for and dwell positions were defined consecutively. The transit time is accounted for in (c). The measured dwell time with and without transit correction is shown in (d). Dashed lines indicate the planned dwell times were added to guide the eyes. (Table 1—experiment 1.)

**Table 2.** Dwell times measured with different acquisition rates for two distances between the IP and phantom surface. Results represent the mean value  $\pm \sigma$  (Type A, standard deviation). No relevant difference was observed for results obtained with low and high-resolution. LR = low-resolution 0.0278 cm pixel size.

Distance (cm)	Planned dwell time (s)	Difference between planned and measured dwell times (s) for the different acquisition rates (LR)							
		5 fps		9 fps		20 fps		33 fps	
		Mean $\pm 1\sigma$	Max.	Mean $\pm 1\sigma$	Max.	Mean $\pm 1\sigma$	Max.	Mean $\pm 1\sigma$	Max.
10	0.3	—	—	0.00 $\pm$ 0.05	0.1	0.00 $\pm$ 0.01	0.1	0.00 $\pm$ 0.02	0.1
	0.5	0.01 $\pm$ 0.10	0.3	0.00 $\pm$ 0.06	0.1	0.00 $\pm$ 0.01	0.1	0.00 $\pm$ 0.02	0.1
	1.0	0.01 $\pm$ 0.07	0.2	0.01 $\pm$ 0.01	0.1	0.02 $\pm$ 0.03	0.1	0.02 $\pm$ 0.05	0.3
20	0.3	—	—	0.00 $\pm$ 0.05	0.1	0.00 $\pm$ 0.01	0.1	0.01 $\pm$ 0.01	0.2
	0.5	0.01 $\pm$ 0.07	0.3	0.00 $\pm$ 0.06	0.1	0.00 $\pm$ 0.01	0.1	0.01 $\pm$ 0.02	0.5
	1.0	0.01 $\pm$ 0.07	0.2	0.01 $\pm$ 0.04	0.1	0.01 $\pm$ 0.03	0.1	0.01 $\pm$ 0.04	0.5

Table 2 shows a comparison between planned and measured dwell times. Differences are below 0.1 s for most of the dwell positions reaching a maximum of 0.5 s for the highest acquisition rate (33 fps) due to the low response of the IP for such a high acquisition rate. The highest differences above 0.1 s were also observed for 5 fps where the acquisition time per frame is 0.2 s. The processing time is much lower (tenfold) than the acquisition rate so the data can be processed in real-time.

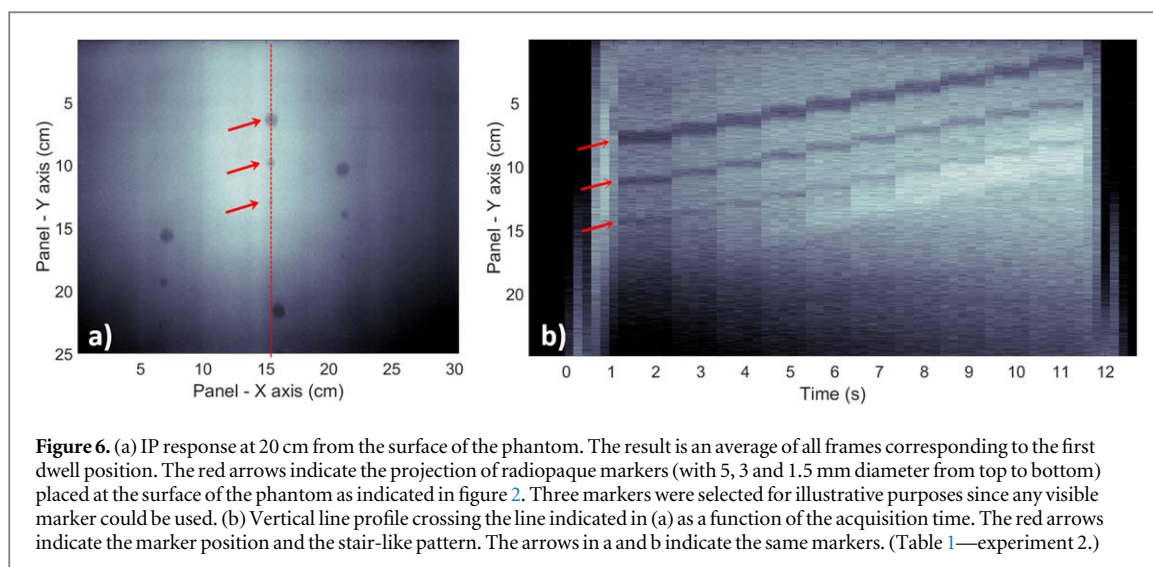


**Figure 6.** (a) IP response at 20 cm from the surface of the phantom. The result is an average of all frames corresponding to the first dwell position. The red arrows indicate the projection of radiopaque markers (with 5, 3 and 1.5 mm diameter from top to bottom) placed at the surface of the phantom as indicated in figure 2. Three markers were selected for illustrative purposes since any visible marker could be used. (b) Vertical line profile crossing the line indicated in (a) as a function of the acquisition time. The red arrows indicate the marker position and the stair-like pattern. The arrows in a and b indicate the same markers. (Table 1—experiment 2.)

### 3.2. Image registration and dwell positions

#### 3.2.1. Radiopaque markers

##### 3.2.1.1. Marker size

Figure 6(a) shows the IP response for an irradiation with the phantom surface at 20 cm from the panel.

Figure 6(b) shows a vertical line profile (crossing the three indicated markers) as a function of the acquisition time. The projection of the markers creates a stair-like pattern (the pattern can vary depending on the source trajectory). Similarly to the method described in section 2.3, where differences in the IP response were used to identify the time interval corresponding to dwell positions, the displacement of the marker projections can also be used to detect source position and dwell time intervals as an alternative method. Markers in figure 6(b) are not clearly visible when the source is approaching the first dwell position (before  $\approx 1.2$  s) and when returning to the safe (after  $\approx 11.5$  s). The marker with 0.3 cm diameter was selected since its projection is well defined and its size still reasonably small to avoid discomfort to the patient in a future clinical application.

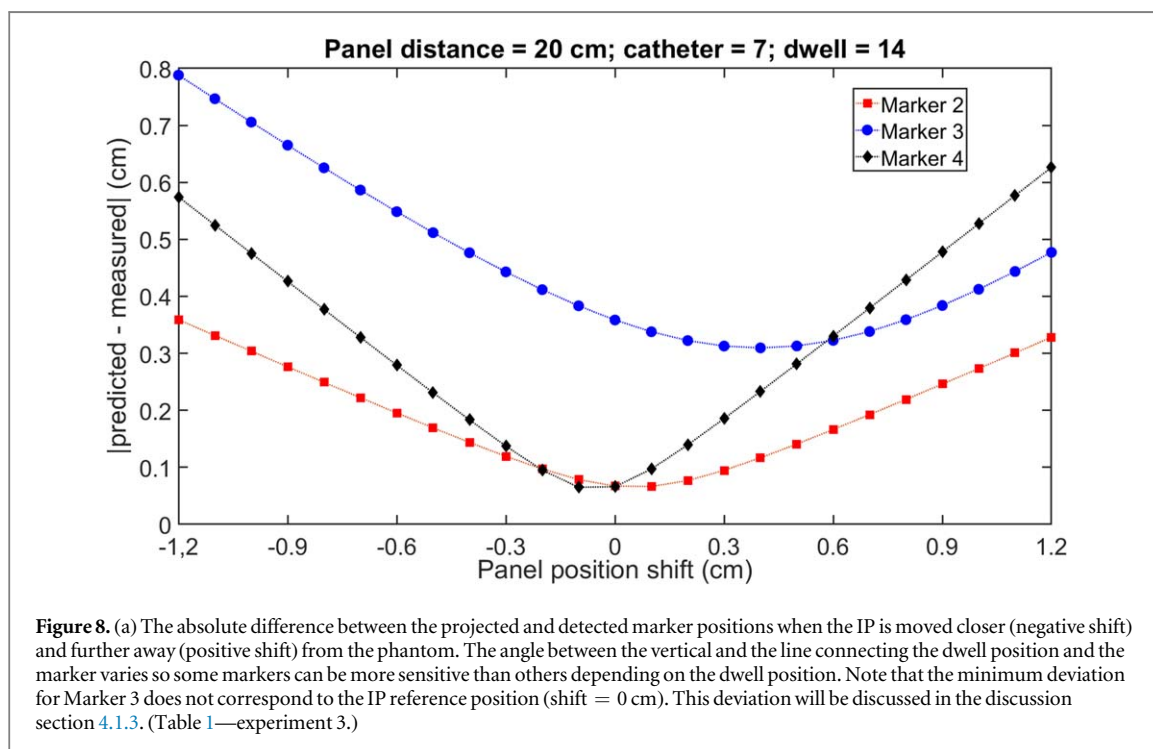
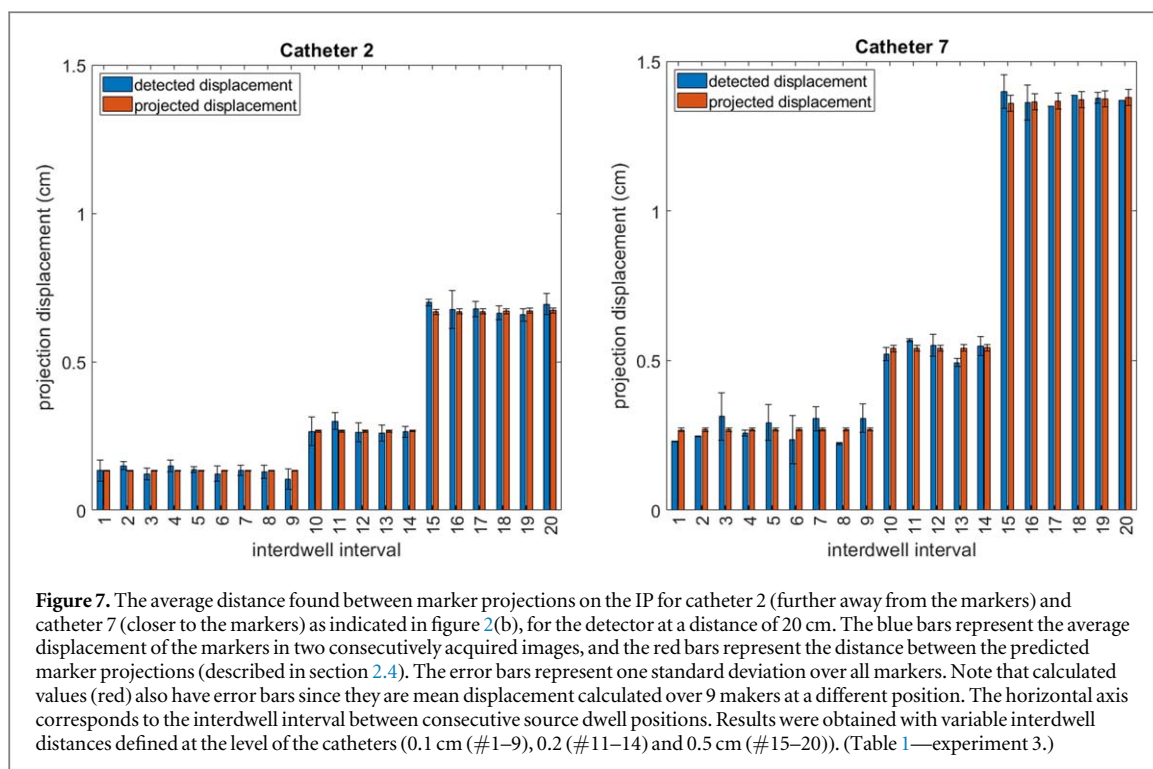
##### 3.2.1.2. Image registration and interdwell distances

The marker-finding algorithm was applied to the IP frames. The detection of the patient markers, used for image registration, depends on their position in relation to the source since some projections are outside the detector area or less visible in regions with low contrast near the edges of the panel. The effectiveness of the marker detection algorithm ranged from 71% up to 98% for acquisitions performed with channels 2 and 7, respectively (figure 2(b)). Results obtained with the panel at 20 cm from the phantom are slightly worse since fewer markers are visible (more projections lie outside the panel with larger distances between the panel and the source). In 99% of all dwell positions, the IP missed two or fewer markers, where approximately 9.2 and 5.5 markers were expected to be in the field-of-view for 10 and 20 cm phantom detector distance, respectively.

Figure 7 shows the measured shift of the marker projection for consecutive dwell positions compared to the predicted marker displacement. The mean difference between predicted and measured marker displacement (at the level of the IP) is  $0.02 \pm 0.02$  cm (1 STD). The magnitude of the marker projection shift due to a 0.1 or 0.2 cm source movement is much larger than the standard deviation. The marker projection displacement was also evaluated by simulating varying distances between the IP position and the surface of the patient as shown in figure 8. Marker projections near the edges of the IP are more sensitive (visible differences for a 0.2 mm shift) to changes as can be seen by the difference in the slope between marker 2 and 3. The marker sensitivity to variations in the distance between the panel and the surface of the phantom depends on the dwell position with sensitivity increasing for larger angles.

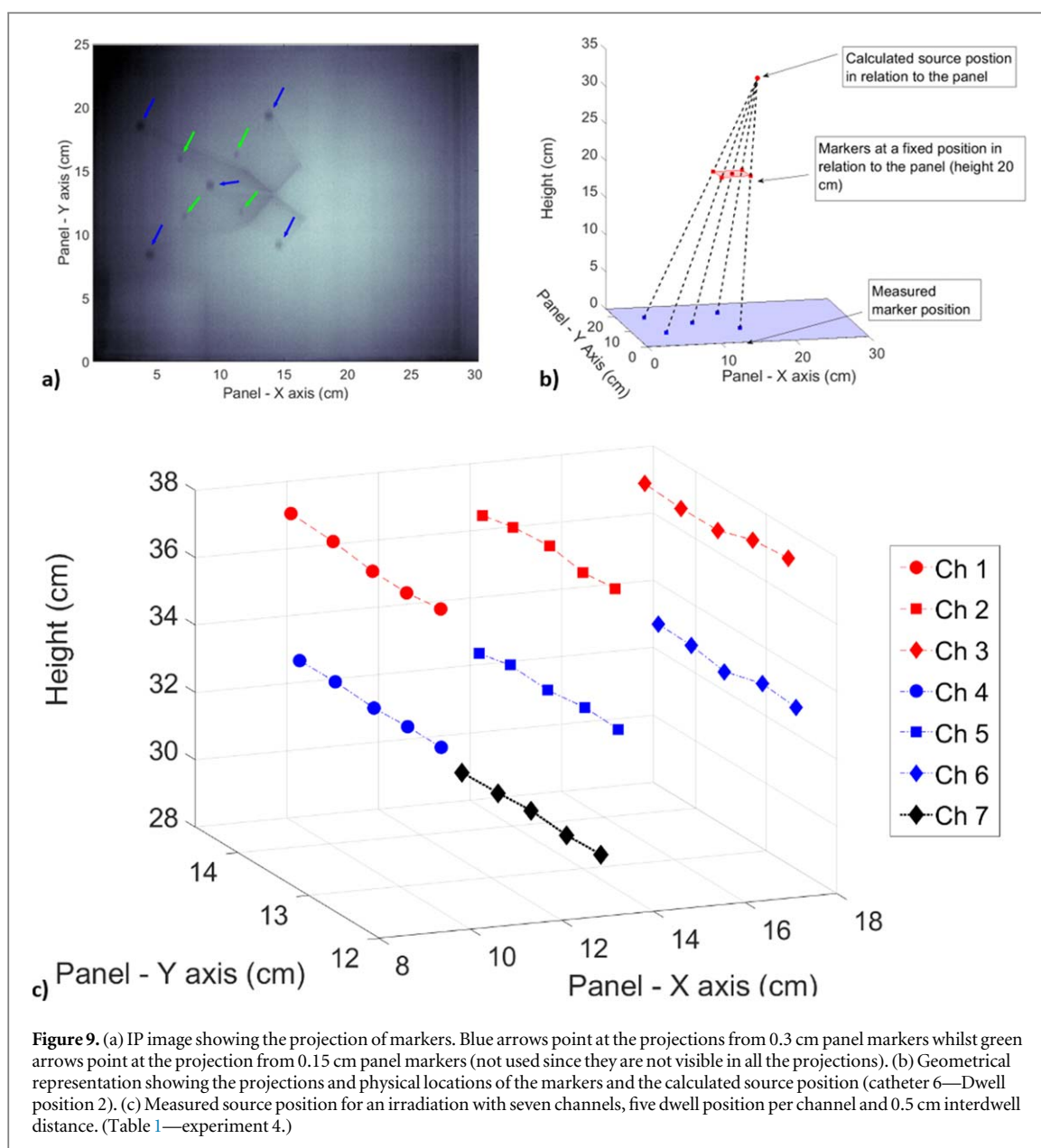
##### 3.2.2. Dwell position

Figure 9 shows an IP frame obtained with markers at known positions related to the panel, an illustration of the backprojection method, used to calculate the source position, and the calculated dwell positions for a seven channel-implant with five dwell positions each. The measured interdwell distance mean deviation was  $0.02 \pm 0.03$  cm (1STD) with a maximum deviation of 0.08 cm for both 0.2 and 0.5 cm interdwell distances. The absolute position of the tip of each catheter showed a maximum offset of 0.1 cm. The maximum deviation between each dwell position and the tip of the catheter was 0.08 cm for both 0.2 and 0.5 cm interdwell distances. The distance between the catheters also showed a maximum deviation below 0.1 cm.



### 3.2.3. Tissue mimicking materials

The boundaries of the phantom are visible (figure 10(a)), where the edges of a cortical bone insert can also be visualized (figure 10(b)). Bone and lung inserts can be visualized by adjusting the contrast, whilst soft tissues (e.g. muscle and adipose tissue) cannot be distinguished without additional postprocessing (e.g. normalization or background subtraction). Figure 10(b) (black arrow) shows a response variation that is most likely due to the geometry of the phantom (figure 4) since its shape (similar to a patient) results in different attenuations depending on the path between the source and the panel. The IP responses obtained for different TMIs (one insert irradiated at a time), normalized to the response obtained with the solid water insert are shown in figures 10(c), (d). Response ratios vary from 0.94 (cortical bone) up to 1.06 (lung insert) with smaller differences observed for soft tissues and lower density bone inserts. The center of the insert projection (obtained with a

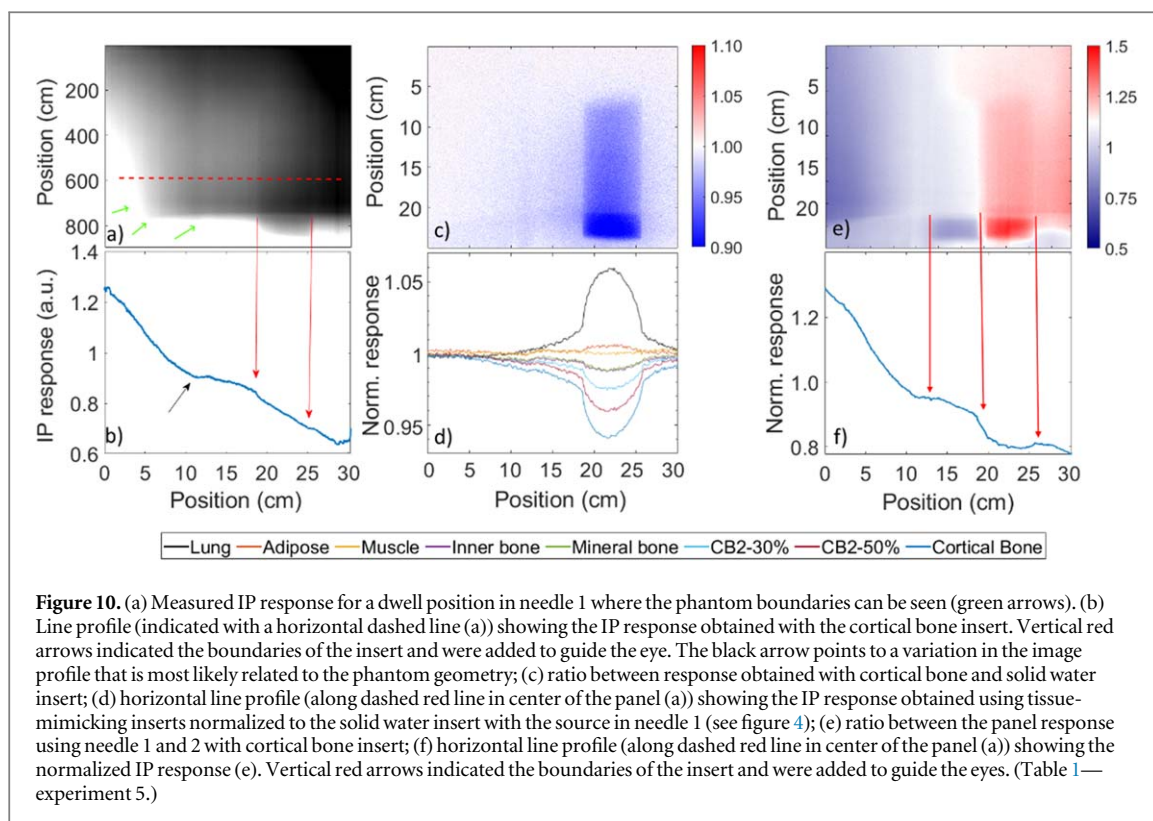


Gaussian fit applied to the intensity profiles as illustrated in figure 10(d) shows a  $\pm 5.5$  cm shift for needles 1 and 3 when compared to the projection obtained using needle 2 at the center. Figures 10(e), (f) shows the result obtained with the source in channel 1 normalized to the result obtained in channel 2 using a cortical bone insert. This approach enhances the visualization of the TMIs creating more noticeable patterns in the profile (figure 10(f)). The projection of the bone insert on the panel depends on the source position, which was highlighted by the normalization. This approach enhances image quality allowing the detection of the inserts for lung and all bone inserts.

#### 4. Discussion

Future directions and requirements for *in vivo* dosimetry in brachytherapy were recently published describing the advantage of time-resolved dosimetry for source tracking (Fonseca *et al* 2020). Previous studies have shown promising results using 2D detectors on phantoms (Bati *et al* 2010, Espinoza *et al* 2013, Smith *et al* 2013, Safavi-Naeini *et al* 2015). One of the main disadvantages of these methods is that source positions are usually acquired in relation to the detector and not the patient anatomy. Therefore, imaging (especially in-room) could improve the accuracy of treatment verification techniques. A clinical trial (Smith *et al* 2018) using x-ray images just before the treatment to create reference images for 2D treatment verification with an IP showed the feasibility of using dummy markers within the catheter. However, the use of an external x-ray device only allows for 2D verification





whilst the use of the  $^{192}\text{Ir}$  gamma rays proposed in this work allows for 3D reconstructions. Therefore,  $^{192}\text{Ir}$  gamma for imaging (Verhaegen *et al* 2007) during the treatment can overcome some technical limitations and could be combined with other conventional imaging modalities of in-room imaging (e.g. CT).

Source tracking has also been performed using multiple point detectors (Kertzschner *et al* 2014, Wang *et al* 2014, Johansen *et al* 2018) and electromagnetic tracking (Reniers *et al* 2012, Tho and Beaulieu 2019) showing high precision determining dwell times and positions. However, more studies are necessary to determine the sensitivity and specificity of different IVD methods.

In this section, we follow the recommendations (Fonseca *et al* 2020) including information about treatment errors that could be detected, impact in the workflow, observed uncertainties and limitations of the proposed approach.

#### 4.1. Uncertainties and limitations

Results obtained with 10 and 20 cm distance between the phantom surface and the IP were similar for all the evaluated positions. Magnification effects can be different as discussed below, but no major differences in performance of IrIS were observed.

##### 4.1.1. Dwell times

The IP used in this study has several acquisition modes and different acquisition rates that influence the results. Low acquisition rates (e.g. 5 fps) did not detect all the dwell positions whilst high acquisition rates (e.g. 33 fps) resulted in very low intensity signals making it difficult to distinguish dwell positions resulting in larger dwell time deviations (up to 0.5 s) than results obtained with 20 fps (up to 0.1 s). The time measurement uncertainty was estimated, considering the standard deviation of the measurements and the acquisition rate, as the acquisition time of one frame (e.g. 20 fps has an acquisition time of 0.05 s and therefore the uncertainty is estimated as 0.05 s). In addition, the software developed for automatic source detection requires that the source remains static for at least two consecutive frames to detect a dwell position. If the user aims to measure a 0.30 s dwell time, a minimum acquisition rate of 0.15 s ( $\approx$  7 fps) will be required. However, the actual dwell time is shorter than the planned dwell time due to transit time correction (Brauer and Ferguson 2015, Bellezzo *et al* 2019). Figure 5 shows that the peaks used to identify dwell positions are not as pronounced when acquired with 9 fps as when acquired with 20 fps indicating that acquisition rates lower than 9 fps may not be suitable for the measurement of such a short dwell time.

The dwell time detection algorithm cannot account for differences between patient and source motion. Therefore, if the patient moves the software will detect a new dwell position even if the source remains at the

same position in relation to the patient. This then could yield a false positive error warning that we aim to mitigate by using radiopaque markers to identify patient translations and rotations. This issue could also be solved by further exploring the combination of panel markers and patient markers (might be subject to larger uncertainties) or by combining IP acquisition with a patient tracking system (e.g. a camera system) that can be used to distinguish between patient and source motion. In addition, communication between the afterloader and IrIS could provide information about the exact moment when the source is expected to move.

#### 4.1.2. Dwell positions and interdwell distances

Earlier publications suggested mathematical fits to signals from IPs to derive the three-dimensional Cartesian coordinates of the dwell positions. (Smith *et al* 2013, Fonseca *et al* 2017a) Although results were very promising using water phantoms close to the IP, the method is not very suitable for this experimental setup, mimicking a patient. Preliminary analysis of the data (not shown) shows that for the distances used in this study the IP response does not show a very pronounced peak so mathematical fits are not accurate as observed in previous studies (Smith *et al* 2013, Fonseca *et al* 2017a) with an IP closer to the surface of a water phantom. In addition, photons leaving the body cross different amounts of 'tissue' and air leading to the projection of the body boundaries (figure 10(a)) and creating some high-intensity regions that can shift the results of mathematical fits applied to the IP images. The same effect occurs due to a relatively high amount of scatter coming from the edge of the IP. The use of markers on the phantom or at a fixed position near the IP seems to be a more robust and direct solution that is also less sensitive to scatter (discussed in section 4.2). The markers at known positions (e.g. attached to a holder above the panel or to the treatment table) related to the panel allow the 3D reconstruction of the dwell positions with submillimeter accuracy so interdwell distances, the distance between catheters, and the delivery order can be verified. The displacement of individual needles would be detected whilst the displacement of the whole implant would not be detected as an error since source positions are measured in relation to the panel and not to the patient anatomy. This issue can be solved by combining markers at fixed positions in relation to the panel with markers on the patient.

Markers on the surface of the phantom were used to verify interdwell distances. The comparison between the predicted and measured marker projections is an accurate method to verify interdwell distances. As shown in figure 7, even a 0.1 cm difference in the dwell position results in a measurable shift in the marker projections on the IP. The standard deviation of the difference between detected and predicted marker positions ( $\pm 0.02$  cm) is much smaller than the minimum interdwell distance (0.1 cm) allowed by the afterloader. The distance between the markers (surface of the phantom) and the IP leads to a magnification effect, discussed in the next section, that increases the accuracy of the method. Interdwell distances were calculated based on dwell position measurements using panel markers fixed to a holder at a fixed distance (20 cm) from the IP showing submillimeter accuracy.

#### 4.1.3. Image registration

Radiopaque markers are clearly visible in the IP images, with automatic detection working well for a marker with a diameter of 3 mm. Smaller markers can be detected but misdetection due to noise is considerable and requires manual inspection of the detected positions, which is not possible for thousands of frames. As the markers are visible on both planning CT and IP images they can be used for image registration defining the patient position (using the CT as reference) in relation to the IP. As a first step, we propose to use the prediction of the patient marker projections, based on the CT image, using IrIS to perform rigid registration.

The main component of the overall uncertainty, considering only the patient marker projection and ignoring possible variations between imaging and treatment stages, comes from the definition of the CT coordinates of the radiopaque markers due to a magnification effect that can highlight differences in dwell positions (useful to detect errors) but also magnifies the uncertainties in the patient marker position. It was estimated that the reference marker position defined using a CT scan has an accuracy of  $\pm 0.1$  cm which is magnified in the projection on the IP. The subsequent uncertainty in the projection position was estimated by shifting the marker position in the treatment plan for interdwell time verification (see table 1) and recalculating the projected positions on the panel using IrIS. The patient marker projection uncertainty varies from 0.17 cm for catheter 1–3 (figure 2) up to 0.24 cm for catheter 7 (closer to the markers) for a panel distance of 10 cm from the phantom. Differences up to 0.40 cm were observed with the panel at 20 cm from the surface of the phantom. Figure 8 shows that marker 3 has the worst agreement for catheter 7 which is consistent with the reported uncertainties. The uncertainties are smaller for measurements with the panel at  $45^\circ$  and  $90^\circ$  (minimum uncertainty  $\approx 0.1$  cm) than at  $0^\circ$ . This is caused by the larger distances between the source and the patient markers at  $45^\circ$  and  $90^\circ$  so that less magnification occurs (figure 2), but this also means the IP response is worse. Therefore, the IP position around the patient could be optimized to minimize registration uncertainties.

The image registration uncertainty (considering only the marker projection) goes from 0.1 cm up to 0.4 cm depending on the catheter adopted for reference. Therefore, the minimum uncertainty for the position of the

**Table 3.** Examples of treatment errors that could be detected using the proposed method including the detection phase (e.g. within the same dwell position, after each dwell position or after each channel or after the treatment).

Treatment error	Detection phase	Expected accuracy
Dwell time deviations	Dwell times are continually monitored so an alarm can be triggered as soon as the difference reaches a user-specified threshold	Differences as low as 0.1 s could be detected. However, transit time corrections and measurement uncertainties could lead to a large number of false positives with questionable clinical impact
Interdwell distance deviations	Interdwell distances are calculated after each dwell position starting from the second dwell position of each catheter onwards	High accuracy (better than 0.1 cm) can be obtained since it is a relative measurement
Swapped catheters	(1) A swapped catheter would lead to marker projections that will not match the predicted positions by using rigid registrations. The error could be detected after the first dwell position  (2) If a predicted image (e.g. ray tracing) including anatomical information is available, the error could be detected after the first dwell position  (3) Position measurements in relation to the IP could detect the error when the source moves to the second channel. As this is a relative measurement, data from more than one channel needs to be acquired before performing this analysis	(1) The accuracy of the marker projection prediction depends on the source position varying from 0.1 up to 0.4 cm for the evaluated cases. IrIS can be used to calculate projection uncertainties to support the definition of warning or action thresholds (most likely a few millimeters)  (2) The detection based on anatomical features would be less susceptible to variations as the marker detection. However, it is not possible to estimate the accuracy of the method based on the current results  (3) Dwell position measurements in relation to the IP are more accurate than results obtained with marker projection so swapped catheters can be detected even if the swapped catheters are only 0.1 or 0.2 cm apart
Dwell position deviation	The same detection phases described for the swapped catheter apply to this item (both are dwell position deviations). Note that shifts of the whole implant could only be detected by using the markers with a fixed position (1) or anatomical information (2). Relative measurements (3) cannot detect a shift of the whole implant	(1) Similar accuracy as the previous item (swapped catheters)  (2) Similar accuracy as the previous item (swapped catheters)  (3) 0.1 or 0.2 cm offsets can be detected. However, no error would be detected if the whole implant shifts
Additional errors	Deviations in the number of dwell positions per channel, number of channels, irradiation time per channel, total irradiation time, needle offsets, order of the dwell positions	

patient in relation to the IP is 0.1 cm (IP at 45° and 90°) and 0.2 cm (IP at 0°). Note that this uncertainty applies to absolute positions in relation to the planning CT since relative measurements (e.g. interdwell distances) are more accurate as discussed in the previous section. The registration could be continuously improved during the treatment by averaging registration coordinates obtained with different catheters as the treatment progresses.

The accuracy of the method depends on the number of markers (e.g. information from multiple markers could be averaged reducing the uncertainties), the position of the IP in relation to the patient, and the position of the markers in relation to IP and dwell positions. Therefore, uncertainties are patient- and dwell position-specific.

#### 4.2. Anatomical information

This study shows that the IP is sensitive to the material between the source and the IP and can display phantom boundaries depending on the IP position (figure 10). This information is of interest since the IP can provide anatomical information and track the source simultaneously. The projection of anatomical structures with a high density, like bone, could be used for image registration and to verify the source position in relation to the patient anatomy. However, the IP results are dominated by the scatter contribution with limited features visible (e.g. phantom contour in figure 10) to human eyes. Response enhancement is possible with post-processing or using ratios between measured frames (e.g. tissue responses were normalized to the measurement performed with the solid water insert), which is not possible for a patient. However, the subtraction of images from 2 dwell position (figures 10(e), (f)) enhanced the image allowing the visualization of TMIs inserts with low and high densities (lung bone materials), which would be theoretically possible in patients.

The results are a proof of concept and further research is necessary to extract and use anatomical information measured by the IP. Verhaegen *et al* (2007) evaluated scattering interactions for different phantoms and showed reduced contrast for imaging objects with the  $^{192}\text{Ir}$  source within the phantom. Scatter corrections commonly applied to cone beam CT imaging (van der Heyden *et al* 2020) could also improve IP image quality for  $^{192}\text{Ir}$  enhancing anatomical features. Ray-tracing or Monte Carlo simulation could be used to create predicted images with primary photons only, based on the patient's anatomy, to compare its features to those of acquired images, corrected for scatter. Figure 10(b) shows some patterns that could be used for comparison.

The transrectal US probe was in place during all the experiments to mimic realistic HDR prostate treatments and to evaluate a possible shielding effect as described by Poder *et al* (2019). No drastic attenuation of the signal due to the US probe was observed. However, the effect of the US probe was not evaluated in this study and could be of potential interest for future research.

#### 4.3. Impact on the workflow and error detection

The brachytherapy workflow consists of several manual steps which can be very stressful for a department, and sensitive for errors. Therefore, treatment verification methods should have a minor impact, increase the safety level and provide sufficient accuracy that can benefit the patient and justify its clinical implementation. IrIS is a completely non-invasive system that should have only a minor impact on the workflow (e.g. placement of radiopaque markers). More research is needed to define the optimal markers positions. IrIS automatically imports all the information from the treatment planning system and can automatically start recording frames once radiation is detected. Nevertheless, a treatment verification system can lead to alarms indicating errors that would require further investigations and resources. At this stage, it is not possible to provide quantitative information about the impact of alarms, including false positives.

The results obtained in this study indicate that IrIS is capable of verifying clinically relevant parameters. The information can be combined to detect several treatment errors, to suggest corrective actions, and also to provide accurate information about dose delivery allowing dose recalculations that could lead to interfraction adaption or better outcome assessment for tumor control and normal tissue response. Table 3 lists some treatment errors that could be detected based on the results described in this paper and previous experiences with this type of detectors (Fonseca *et al* 2017a, 2017b). Note that error detection sensitivity and specificity depends on several factors including, but not limited to, detector accuracy, clinical action thresholds, delivery uncertainties and magnitude of the error (Fonseca *et al* 2020) that should be evaluated for each type of error. Additional uncertainties due to motion, including internal intrafractional organ motion, is a potential source of uncertainty that requires further research.

## 5. Conclusion

The proposed proof of concept of a brachytherapy treatment verification system (IrIS) can combine source tracking with anatomical gamma-ray imaging without exposing the patient to any additional radiation dose. The use of radiopaque markers and anatomical information can solve one of the main limitations of source tracking systems that measure the source position in relation to the detector and not to the patient. Such a system would have a minimal impact on the workflow and benefit the brachytherapy patient by early detection of errors and measuring the true delivered dose to the patient. The measurement of dwell times and positions in relation to the panel shows great accuracy whilst the use of markers fixed on the patient and the extraction of anatomical information requires further research to verify the feasibility and quantify uncertainties for clinical cases.

## Acknowledgments

This project was partially supported by Varian Medical Systems. We thank Stavroula Giannuli and Rebecca Park from Varian for commenting on the paper. G P Fonseca and T van Wagenberg were supported by KWF (Grant 12780—Bas Mulder award). We thank Vera Schroen, Janneke Cruys and Esther Visser for their contribution to this project.

## ORCID iDs

G P Fonseca  <https://orcid.org/0000-0002-8087-1193>

T van Wagenberg  <https://orcid.org/0000-0002-5642-510X>



## References

- Alecú R and Alecú M 1999 *In-vivo* rectal dose measurements with diodes to avoid misadministrations during intracavitary high dose rate brachytherapy for carcinoma of the cervix *Med. Phys.* **26** 768–70
- Allahverdi M, Sarkhosh M, Aghili M, Jaber R, Adelnia A and Geraily G 2012 Evaluation of treatment planning system of brachytherapy according to dose to the rectum delivered *Radiat. Prot. Dosim.* **150** 312–5
- Anagnostopoulos G, Baltas D, Geretschlaeger A, Martin T, Papagiannis P, Tselis N and Zamboglou N 2003 *In vivo* thermoluminescence dosimetry dose verification of transperineal 192Ir high-dose-rate brachytherapy using CT-based planning for the treatment of prostate cancer *Int. J. Radiat. Oncol. Biol. Phys.* **57** 1183–91
- Andersen C E, Nielsen S K, Lindegaard J C and Tanderup K 2009 Time-resolved *in vivo* luminescence dosimetry for online error detection in pulsed dose-rate brachytherapy *Med. Phys.* **36** 5033–43
- Astrom L, Grusell E, Sandin F, Turesson I and Holmberg L 2018 Two decades of high dose rate brachytherapy with external beam radiotherapy for prostate cancer *Radiother. Oncol.* **127** 81–7
- Atherton T J and Kerbyson D J 1999 Size invariant circle detection *Image Vis. Comput.* **17** 795–803
- Ballester F, Puchades V, Lluch J L, Serrano-Andrés M A, Limami Y, Pérez-Calatayud J and Casal E 2001 Technical note: Monte-Carlo dosimetry of the HDR 12i and Plus 192Ir sources *Med. Phys.* **28** 2586–91
- Bati M, Burger J, Cindro V and Kramberger G 2010 Verification of high dose rate 192Ir source position during brachytherapy treatment *Nucl. Instrum. Methods Phys. Res. A* **617** 206–8
- Belley M D, Craciunescu O, Chang Z, Langloss B W, Stanton I N, Yoshizumi T T, Therien M J and Chino J P 2018 Real-time dose-rate monitoring with gynecologic brachytherapy: results of an initial clinical trial *Brachytherapy* **17** 1023–9
- Bellezo M, Baeza J A, Voncken R, Reniers B, Verhaegen F and Fonseca G P 2019 Mechanical evaluation of the Bravos afterloader system for HDR brachytherapy *Brachytherapy* **18** 852–62
- Brauer D G and Ferguson K J 2015 The integrated curriculum in medical education: AMEE Guide No. 96 *Med. Teach.* **37** 312–22
- Brezovich I A, Duan J, Pareek P N, Fiveash J and Ezekiel M 2000 *In vivo* urethral dose measurements: a method to verify high dose rate prostate treatments *Med. Phys.* **27** 2297–301
- Carrara M et al 2017 Clinical application of MOSkin dosimeters to rectal wall *in vivo* dosimetry in gynecological HDR brachytherapy *Phys. Med.* **41** 5–12
- Crook J, Marbán M and Batchelar D 2020 HDR prostate brachytherapy *Semin. Radiat. Oncol.* **30** 49–60
- Cygler J E, Saoudi A, Perry G, Morash C and Choan E 2006 Feasibility study of using MOSFET detectors for *in vivo* dosimetry during permanent low-dose-rate prostate implants *Radiother. Oncol.* **80** 296–301
- Das R, Toye W, Kron T, Williams S and Duchesne G 2007 Thermoluminescence dosimetry for *in-vivo* verification of high dose rate brachytherapy for prostate cancer *Australas. Phys. Eng. Sci. Med.* **30** 178–84
- Espinoza A, Beeksmas B, Petasecca M, Fuduli I, Porumb C, Cutajar D, Corde S, Jackson M, Lerch M L and Rosenfeld A B 2013 The feasibility study and characterization of a two-dimensional diode array in ‘magic phantom’ for high dose rate brachytherapy quality assurance *Med. Phys.* **40** 111702
- Fonseca G P, Johansen J G, Smith R L, Beaulieu L, Beddar S, Kertzscher G, Verhaegen F and Tanderup K 2020 *In vivo* dosimetry in brachytherapy: Requirements and future directions for research, development, and clinical practice *Phys. Imaging Radiat. Oncol.* **16** 1–11
- Fonseca G P, Van den Bosch M R, Voncken R, Podesta M and Verhaegen F 2017b A novel system for commissioning brachytherapy applicators: example of a ring applicator *Phys. Med. Biol.* **62** 8360–75
- Fonseca G P, Johansen J G, Smith R L, Beaulieu L, Beddar S, Kertzscher G, Verhaegen F and Tanderup K 2020 *In vivo* dosimetry in brachytherapy: requirements and future directions for research, development, and clinical practice *Phys. Imaging Radiat. Oncol.* **16** 1–11
- Fonseca G P, Podesta M, Bellezo M, Van den Bosch M R, Lutgens L, Vanneste B G L, Voncken R, Van Limbergen E J, Reniers B and Verhaegen F 2017a Online pretreatment verification of high-dose rate brachytherapy using an imaging panel *Phys. Med. Biol.* **62** 5440–61
- Fonseca G P, Reniers B, Landry G, White S, Bellezo M, Antunes P C, de Sales C P, Welteman E, Yoriyaz H and Verhaegen F 2014 A medical image-based graphical platform—features, applications and relevance for brachytherapy *Brachytherapy* **13** 632–9
- Guiral P, Ribouton J, Jalade P, Wang R, Galvan J M, Lu G N, Pittet P, Rivoire A and Gindraux L 2016 Design and testing of a phantom and instrumented gynecological applicator based on GaN dosimeter for use in high dose rate brachytherapy quality assurance *Med. Phys.* **43** 5240–51
- Jaselske E, Adliene D, Rudzianskas V, Urbonavicius B G and Inciura A 2017 *In vivo* dose verification method in catheter based high dose rate brachytherapy *Phys. Med.* **44** 1–10
- Johansen J G, Rylander S, Buus S, Bentzen L, Hokland S B, Sondergaard C S, With A K M, Kertzscher G and Tanderup K 2018 Time-resolved *in vivo* dosimetry for source tracking in brachytherapy *Brachytherapy* **17** 122–32
- Kertzscher G, Andersen C E and Tanderup K 2014 Adaptive error detection for HDR/PDR brachytherapy: guidance for decision making during real-time *in vivo* point dosimetry *Med. Phys.* **41** 052102
- Mason J, Mamo A, Al-Qaisieh B, Henry A M and Bownes P 2016 Real-time *in vivo* dosimetry in high dose rate prostate brachytherapy *Radiother. Oncol.* **120** 333–8
- Melchert C, Soror T and Kovacs G 2018 Quality assurance during interstitial brachytherapy: *in vivo* dosimetry using MOSFET dosimeters *J. Contemp. Brachytherapy* **10** 232–7
- Nose T, Koizumi M, Yoshida K, Nishiyama K, Sasaki J, Ohnishi T and Peiffert D 2005 *In vivo* dosimetry of high-dose-rate brachytherapy: study on 61 head-and-neck cancer patients using radiophotoluminescence glass dosimeter *Int. J. Radiat. Oncol. Biol. Phys.* **61** 945–53
- Poder J, Cutajar D, Guatelli S, Petasecca M, Howie A, Bucci J, Carrara M and Rosenfeld A 2019 A Monte Carlo study on the feasibility of real-time *in vivo* source tracking during ultrasound based HDR prostate brachytherapy treatments *Phys. Med.* **59** 30–6
- Reniers B, Landry G, Eichner R, Hallil A and Verhaegen F 2012 *In vivo* dosimetry for gynaecological brachytherapy using a novel position sensitive radiation detector: feasibility study *Med. Phys.* **39** 1925–35
- Safavi-Naeini M et al 2015 BrachyView, a novel in-body imaging system for HDR prostate brachytherapy: experimental evaluation *Med. Phys.* **42** 7098–107
- Sharma R and Jursinic P A 2013 *In vivo* measurements for high dose rate brachytherapy with optically stimulated luminescent dosimeters *Med. Phys.* **40** 071730
- Smith R L, Hanlon M, Panettieri V, Millar J L, Matheson B, Haworth A and Franich R D 2018 An integrated system for clinical treatment verification of HDR prostate brachytherapy combining source tracking with pretreatment imaging *Brachytherapy* **17** 111–21

- Smith R L, Taylor M L, McDermott L N, Haworth A, Millar J L and Franich R D 2013 Source position verification and dosimetry in HDR brachytherapy using an EPID *Med. Phys.* **40** 111706
- Sturdza A et al 2016 Image guided brachytherapy in locally advanced cervical cancer: improved pelvic control and survival in RetroEMBRACE, a multicenter cohort study *Radiother. Oncol.* **120** 428–33
- Suchowerska N, Jackson M, Lambert J, Yin Y B, Hruby G and McKenzie D R 2011 Clinical trials of a urethral dose measurement system in brachytherapy using scintillation detectors *Int. J. Radiat. Oncol. Biol. Phys.* **79** 609–15
- Tanderup K, Christensen J J, Granfeldt J and Lindegaard J C 2006 Geometric stability of intracavitary pulsed dose rate brachytherapy monitored by *in vivo* rectal dosimetry *Radiother. Oncol.* **79** 87–93
- Tho D and Beaulieu L 2019 Technical note: identification of an optimal electromagnetic sensor for *in vivo* electromagnetic-tracked scintillation dosimeter for HDR brachytherapy *Med. Phys.* **46** 2031–6
- Toye W, Das R, Kron T, Franich R, Johnston P and Duchesne G 2009 An *in vivo* investigative protocol for HDR prostate brachytherapy using urethral and rectal thermoluminescence dosimetry *Radiother. Oncol.* **91** 243–8
- van der Heyden B et al 2020 A Monte Carlo based scatter removal method for non-isocentric cone-beam CT acquisitions using a deep convolutional autoencoder *Phys. Med. Biol.* **65** 145002
- Valentin J and International Commission on Radiation Protection 2005 Prevention of high-dose-rate brachytherapy accidents. ICRP Publication 97 *Ann. ICRP* **35** 1–51
- Vanneste B G, Van Limbergen E J, van Lin E N, van Roermund J G and Lambin P 2016 Prostate cancer radiation therapy: What do clinicians have to know? *BioMed Res. Int.* **2016** 6829875
- Verhaegen F, Palefsky S, Rempel D and Poon E 2007 Imaging with Iridium photons: an application in brachytherapy *Proc. SPIE* **6510** 65103S
- Waldhausl C, Wambersie A, Potter R and Georg D 2005 *In-vivo* dosimetry for gynaecological brachytherapy: physical and clinical considerations *Radiother. Oncol.* **77** 310–7
- Wang R, Ribouton J, Pittet P, Guiral P, Jalade P and Lu G N 2014 Implementation of GaN based real-time source position monitoring in HDR brachytherapy *Radiat. Meas.* **71** 293–6
- Zaorsky N G, Davis B J, Nguyen P L, Showalter T N, Hoskin P J, Yoshioka Y, Morton G C and Horwitz E M 2017 The evolution of brachytherapy for prostate cancer *Nat. Rev. Urol.* **14** 415–39